Journal Pre-proof

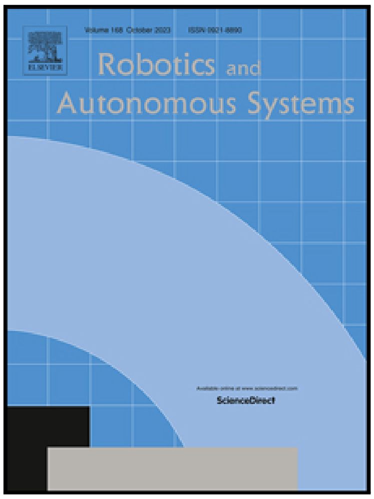

A Novel Versatile Mechanical Integrated Leg-Based Underwater Grasping Function for a Bionic Amphibious Spherical Robot

Chengchao Gu , Shuxiang Guo , Chunying Li , He Yin , Ao Li

PII: S0921-8890(26)00211-3
DOI: https://doi.org/10.1016/j.robot.2026.105539
Reference: ROBOT 105539

To appear in: *Robotics and Autonomous Systems*

Received date: 20 December 2024
Revised date: 14 April 2026
Accepted date: 11 May 2026

Please cite this article as: Chengchao Gu , Shuxiang Guo , Chunying Li , He Yin , Ao Li , A Novel Versatile Mechanical Integrated Leg-Based Underwater Grasping Function for a Bionic Amphibious Spherical Robot, *Robotics and Autonomous Systems* (2026), doi: https://doi.org/10.1016/j.robot.2026.105539

A Novel Versatile Mechanical Integrated Leg-Based Underwater Grasping Function for a Bionic Amphibious Spherical Robot

Chengchao Gu[1], Shuxiang Guo[1, 2,3*], Chunying Li [3*], He Yin[1], Ao Li[1]

1. Key Laboratory of Convergence Medical Engineering System and Healthcare Technology, the Ministry of Industry and Information Technology, Beijing Institute of Technology, Beijing 100081, China.

2. The Department of Electronic and Electrical Engineering, Southern University of Science and Technology, Shenzhen, Guangdong 518055, China

3. The Advanced Institute for Ocean Research, Southern University of Science and Technology, Shenzhen, Guangdong, 518055, China

**Corresponding authors: guo.shuxiang@sustech.edu.cn, licy@sustech.edu.cn*

Abstract

The development of robots equipped with grasping capabilities for ocean exploration and shallow water collection is a crucial research area, where amphibious robots stand out as an ideal platform due to their ability to switch between aquatic and terrestrial locomotion. In this study, we introduce a novel multi-functional mechanical leg, integrated with a mechanical claw device, designed specifically for bionic amphibious robots. The leg features a parallelogram-deformation-contraction structure (PDCS), and its design was followed by a rigorous validation of the selected material's structural strength through static stress analysis. A comprehensive kinematic analysis was also conducted to assess the effective workspace. Experimental results, obtained using the 3D-printed PDCS-equipped mechanical leg, revealed a maximum grasping force of 22.5 N and efficient underwater mobility with a 6 N load. The grasping success rate, aided by manual positioning, consistently surpassed 90%, indicating impressive grasping adaptability. Furthermore, the robot's ability to crawl on land was also confirmed.

Keywords: Amphibious spherical robot, multi-functional robot, integration, mechanical leg, underwater grasping structure.

1. Introduction

In shallow-water operations and marine exploration, the prolonged physiological burden on divers has made robotic replacement technologies a prominent research focus [1]-[2]. A plethora of Underwater Vehicle-Manipulator Systems (UVMS) have been studied and developed [3]-[5], encompassing robots integrating rigid manipulators [6], flexible manipulators with mobile units [7]-[8], and humanoid robots

[9]. Nevertheless, these systems typically depend on ships or other vehicles for transportation and underwater deployment, and lack the ability to transition from land to water autonomously while executing grasping tasks. Therefore, the development of robotic systems that can autonomously traverse the land-water interface and execute underwater grasping tasks holds substantial breakthrough significance. Amphibious spherical robots, leveraging their inherent capability for dual-environment locomotion, offer an ideal platform for this objective.

Consequently, amphibious robotic platforms have been increasingly embraced in recent years for their high adaptability to amphibious environments and operational autonomy, with bio-inspired amphibious robots being of particular interest. Researchers have drawn inspiration from an extensive range of natural creatures [10]-[11], including crabs, cockroaches, snakes, turtles, shrimp, lizards, frogs, and crocodiles. Notably, *Baines et al.* developed an amphibious robot with adaptive limb morphing to enhance locomotion efficiency across land-water boundaries [12]. *Liu et al.* proposed a bionic turtle robot with visual-tactile sensing for terrain-aware gait switching [13]. *Gu et al.* established an acoustic communication-based framework for multi-robot cooperation and instruction transmission [14]. *Li et al.* introduced an improved motion control strategy with thrust allocation to strengthen stability under environmental disturbances [11]. *An et al.* developed an underwater obstacle avoidance strategy for spherical robots using an improved velocity obstacle method and ant colony-based 3D path planning [15]. However, research on amphibious robots has primarily focused on single-robot motion mode transition in terrestrial and aquatic environments [12]-[13], underwater motion decision-making and control [4, 5, 11, 16], multi-robot collaboration [2, 17, 18], local communication among multi-robot swarms [19], and the use of various materials for fabricating robots or their components [20]. Despite these advances, integrating grasping capabilities into amphibious robotic platforms remains a significant challenge. Most critically, the integration of grasping functionality directly dictates the extent to which such robots can genuinely substitute for human divers in collection and manipulation operations, and thus constitutes the essential transition of amphibious robots from "mobile platforms" toward "operational platforms".

The underwater environment constitutes one of the primary operational domains for amphibious robots. These robots can achieve grasping functionality through the integration of robotic arms within an UVMS. Previous research on robotic arms has encompassed typical rigid manipulators designed for mechanical or heavy-load tasks, soft elephant-trunk manipulators [21], rigid adjustable soft grippers [22], and soft grippers featuring a light-emitting octopus sucker-type tentacle structure [23], etc. For example, *Liu et al.* developed a soft continuum manipulator with a reinforcement learning-based controller for autonomous underwater grasping of seafood animals [24]. *Nishi et al.* proposed an MR-based teleoperation system with a reaction torque indicator to improve grasping torque regulation and usability for underwater robot arms [25]. *Wan et al.* fabricated three types of soft pneumatic actuators via DLP 3D printing and demonstrated a soft robotic arm capable of underwater grasping and sorting [21]. *Liu et al.* combined a benthic legged robot with a soft manipulator to extend workspace and enable mobile underwater grasping in real-world environments [26]. Summarizing the methodologies for attaining grasping functionality across various manipulator types and enhancing structural integration during the amalgamation of amphibious robots with manipulators represents an effective strategy for realizing integrated grasping capabilities. While some existing UVMSs exhibit commendable grasping characteristics, the integration of the grasping and mobility units remains relatively generic. This issue results in a considerable overall volume and insufficient flexibility and concealment of the robotic system.

In this paper, a novel mechanical leg structure that integrates a grasping mechanism is introduced, thereby proposing the concept of a unified multi-functional mechanical leg. This mechanical leg can be attached to a bionic amphibious spherical robot, equipping it with grasping capabilities while leveraging the robot's versatile abilities to crawl on land and swim in water [27]-[28]. The primary emphasis of this study is on exploring amphibious robotics, with the current limitation being the lack of terrestrial grasping capabilities. Our proposed multi-functional approach within a single structure effectively enhances the flexibility and deals with the concealment deficiencies observed in conventional UVMSs. This constitutes the primary and most significant contribution of this paper. Additionally, a Parallelogram-Deformation-Contraction Structure (PDCS) for the composite design is proposed. By employing this structure, the mechanical leg can efficiently incorporate the grasping mechanism. The terminal end of this structure is designed with a sharp angle, facilitating the scooping of target objects. Moreover, silicone shells have been integrated into the main contact areas of the structure to enhance friction and improve grip during grasping operations.

The rest of this paper is organized as follows: Section II elaborates on the principles underlying the contraction, grasping, and movement of the innovative mechanical leg. Section III presents an analysis of static stress and kinematics pertinent to the newly designed mechanical leg. Section IV details the relevant experimental procedures. Section V comprises the discussion section. Finally, Section VI concludes this paper.

2. Methods

2.1. Grasping Structure Design

Utilizing the mechanical leg as the carrier for the integrated grasping structure, one can readily draw an analogy between the mechanical leg and a finger, where grasping is achieved through the mutual contact of each finger's tips. A method is required that is tailored for scenarios where the grasping structure remains compact when not in use but can extend when needed. In this paper, we introduce the PDCS. The principle of its contraction is illustrated in **Fig. 1**, which $a'b'c'd'$ is inspired by the PDCS of a folding umbrella. Lines $a'f'$ and $c'e'$ intersect at a fixed point d'. When the structure (indicated by the red dashed box) is pulled to move, the M structure drives c'e' to rotate counterclockwise about d', while a'f' rotates clockwise. Upon pulling the structure enclosed by the red dashed box, $c'e'$ is driven to rotate counterclockwise about d', whereas $a'f'$ rotates clockwise.

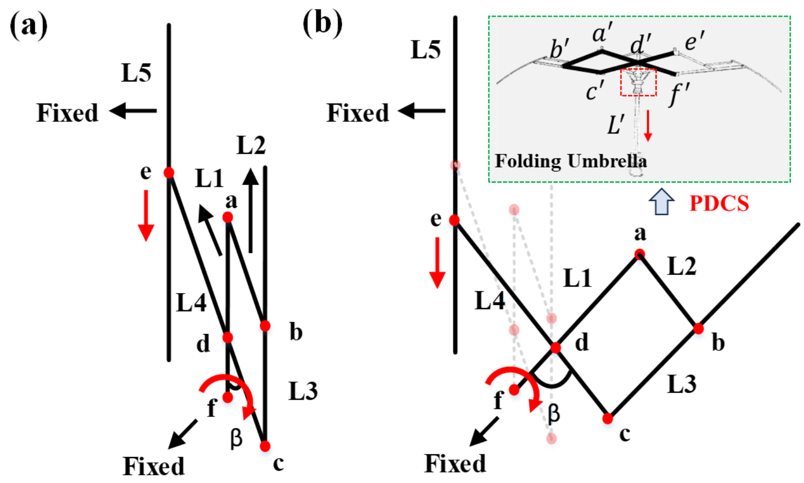

Fig. 1. The simplified structure of mechanical claw: (a) Contraction state; (b) Open state.

Among them, L_1, L_2, L_3, L_4 represent the four connecting rod structures within the PDCS structure. L_5 denotes the sliding rod structure. e serves not only as the endpoint of L_4 but also as a slider component that can move along L_5, thereby restricting and controlling the deformation direction of the contracted structure. Point f represents the schematic location of the servo. a, b, c, d are the connection points for the four links. The positions of L_5 and f remain fixed. When the servo drives the structure to open the grasping mechanism, the L_1 link rotates clockwise around point f. As a result, the entire structure is opened up [29].

In this study, the grasping task was accomplished by driving a pair of opposing mechanical legs within the grasping structure. A detailed introduction of the grasp space formed at the end of the grasping structure is provided below.

The grasping structure terminates in a "three-finger" configuration. The central "finger" features a plate structure with a specific width, while the two lateral "fingers" incorporate a sharp-angled end design instead of a square structure, facilitating effective scooping of the object during grasping. For enhanced functionality, the middle "finger" is strategically positioned either to the left or right of the center, facilitating the interleaving of fingers from a pair of opposing grasping ends during the process of grasping the target object. Additionally, in the in the L_2 rod position, a removable baffle is incorporated to clamp both sides of the target. An upper baffle with a defined width is also added to prevent the object from escaping from the top. Collectively, these elements form a grasping space that envelops the target object in a "box"-like structure.

Furthermore, to address the challenge of grasping a smooth target, this design has undergone a thorough analysis of the primary contact points between the grasping device and the target object, as elaborated in *Section III*. To enhance grip and prevent slippage, silicone rubber casings have been incorporated onto the corresponding parts, as illustrated in **Fig. 2**. It is noteworthy that the "two-finger" located on the outer sides of the "three-finger" structure remain free of silicone sleeves, ensuring a seamless and unobstructed lifting of the object.

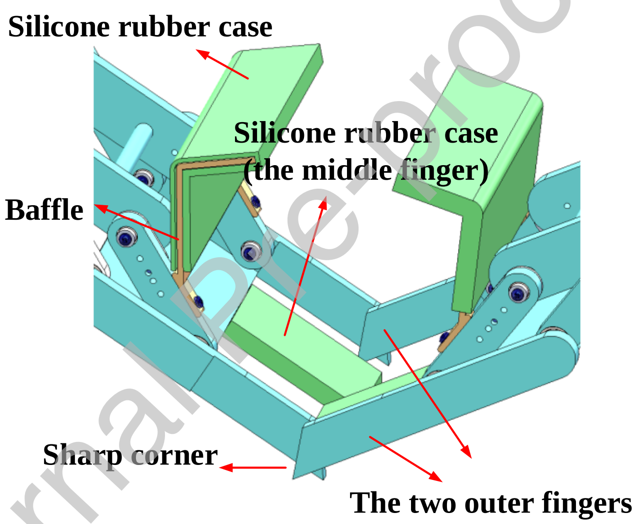

Fig. 2. The details of the clamping structure.

2.2. The Novel Mechanical Leg Design

Regarding the overall structural design of the mechanical leg, we have adopted a three-joint and three-link configuration. The three joints are designated as the "hip," "femur," and "tibia," respectively, with corresponding links named accordingly. The 3D design of the mechanical leg is depicted in **Fig. 3**. It is important to note that the "hip joint" facilitates the leg's horizontal plane swing motion, while the "femur" and "tibia" joints enable vertical plane movement. The mechanical leg is equipped with a thruster, allowing it to perform both land crawling and underwater swimming [30].

The grasping structure is fixed on the "tibia" link with three degrees of freedom and three active joints. The contraction and opening of this structure are directly driven by the "tibia joint". **Fig. 3** (a) illustrates the grasping structure in its contracted state, while **Fig. 3** (b) shows it in its open state. The range of motion for the HC-joint is -45° to 45°, and for the HF-joint, it is -30° to 120°. The grasping structure has a maximum opening angle of 120°. Despite the "finger" structure measuring only 10 cm in length, it is capable of extending up to 17 cm.

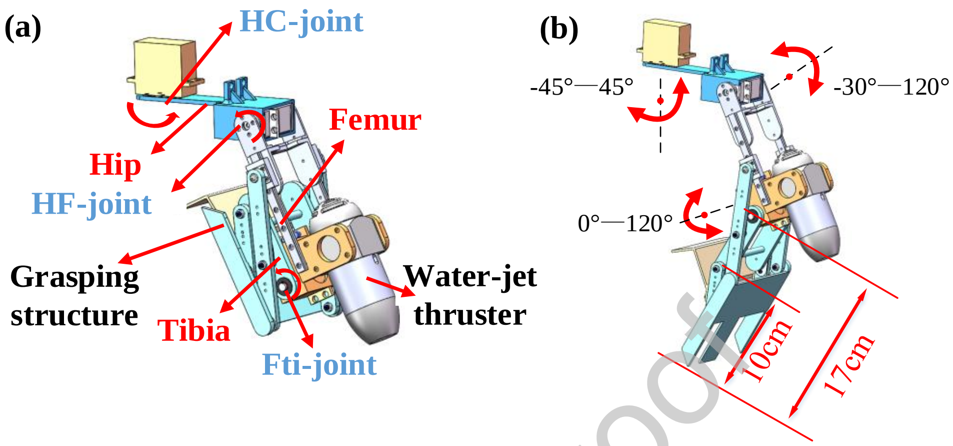

Fig. 3. The details of the mechanical leg: (a) Contraction state; (b) Open state.

The assembly of the mechanical leg structure on the robot is shown in **Fig. 4**. It should be noted that prior to grasping an object, the robot adopts the configuration shown in **Fig. 4** (a), which exemplifies a typical locomotion mode in which four water-jet thrusters generate a resultant force in the desired direction. Once the object is grasped, the robot transitions to the state illustrated in **Fig. 4** (b). In this state, two thrusters supply the primary vertical force, while the other two regulate horizontal movement via swinging and water spraying.

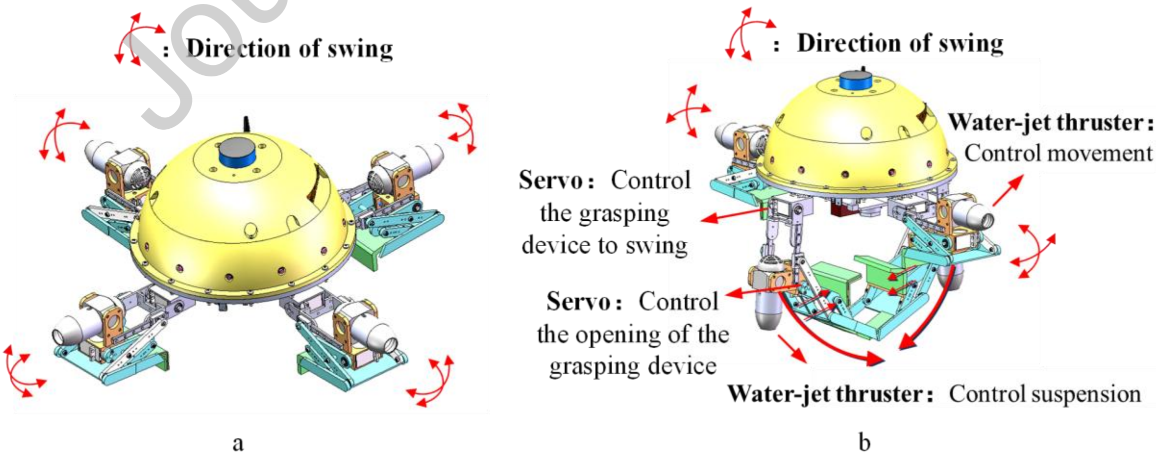

Fig. 4. Schematic depiction of underwater motion states: (a) object in an ungrasped state; (b) object in a grasped state.

2.3. The Locomotive Functions Design

The gait design is inspired by turtle crawling and is illustrated in **Fig. 5**. The motion of the robot primarily depends on the thrusters integrated into its mechanical legs to perform various tasks. Both swimming in water and crawling on roads have been extensively analyzed through theoretical studies in previous robot iterations that lacked the novel structure [29]. During crawling, the entire cycle can be divided into six distinct stages. The dashed section in **Fig. 5** (a) represents the initial leg position. By following the six phases of motion depicted in the image, the robot will advance in the northern direction as indicated.

The improved mechanical leg structure incorporates an active joint to control the retraction of the grasping mechanism. Each mechanical leg can move unidirectionally within a 45° range, see **Fig. 3**. However, because the integration of the grasping mechanism increases the width of the distal end of the mechanical leg to a certain extent, the swing amplitude of the leg must be constrained. In this study, the sum of the angles between adjacent mechanical legs during motion is limited to no more than 40°, which is related to gait of the robot. Namely $\alpha_{\mathrm{leg1}} + \alpha_{\mathrm{leg2}} < 40°$, the rotation direction of leg 1 and leg 2 is shown in **Fig. 5** (a). If the sum of α_{leg1} and α_{leg2} exceeds 40°, collision between the two adjacent legs will occur.

During the swing phase of each leg, the motion of the mechanical leg can be decomposed as illustrated in **Fig. 5** (b). In this figure, the transparent leg joints indicate the positions that the mechanical leg is intended to reach during this phase.

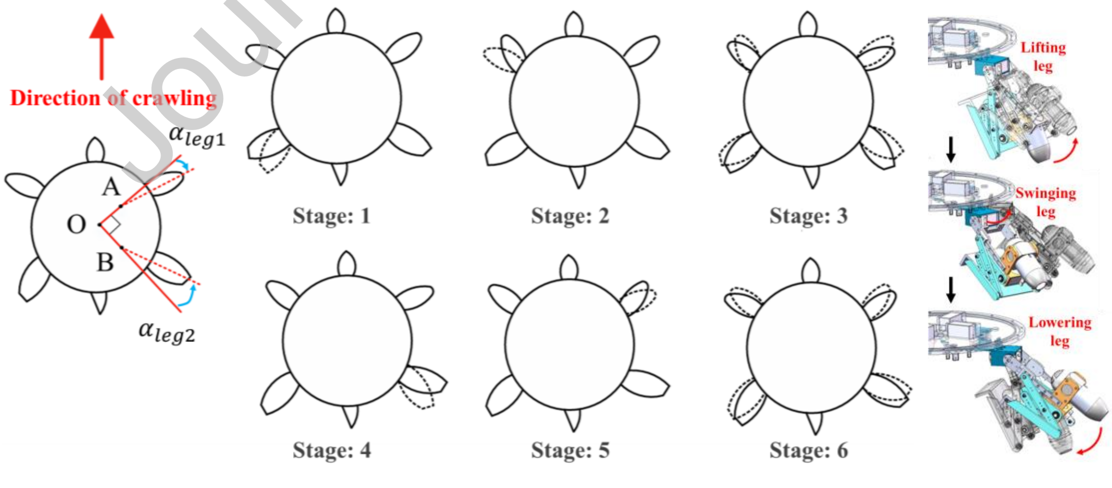

(a) the entire cycle (b) single-leg decomposition

Fig. 5. The schematic diagram illustrating the design of gait.

3. Simulation Analysis

In this section, we have conducted software simulation analyses as outlined in references [25,26].

Initially, we modeled the workspace of the grasping structure, followed by a comprehensive kinematic analysis. Subsequently, the grasping structure underwent a rigorous static stress analysis. Previous research [24] employed metal materials for simulated static stress analysis. However, to precisely replicate the production and application scenarios of the robotic leg, we conducted a reanalysis using ABS material and supplemented it with an additional simulation scenario.

Regarding the software utilized, the structure was designed using SOLIDWORKS 2022. Subsequently, a simplified model file was exported from SOLIDWORKS 2022 and imported into ANSYS software for the completion of the static stress analysis. Additionally, the kinematics analysis of the grasping structure was conducted using Matlab R2016b.

3.1. Kinematic Analysis

Taking into account the three joints of the grasping structure and its three-dimensional workspace, the grasping structure model was simplified for kinematic analysis to assess the workspace for grasping, as depicted in **Fig. 6** (a). The spatial coordinate system for the workspace was established as shown in **Fig. 6** (b). For the theoretical kinematic analysis, the D-H joint parameter method was employed.

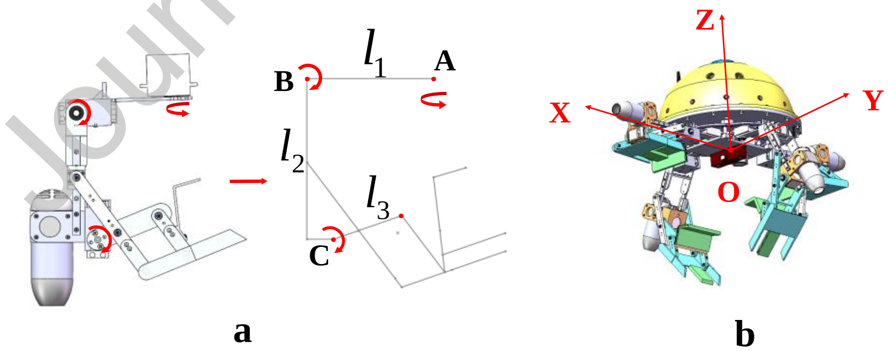

Fig. 6. The figures of workspace: (a) Simplified drawing of the structure; (b)Space coordinate system.

Firstly, we focused on the “tibia” joint. In practical grasping scenarios, the optimal grasping effect was observed when the opening degree was maximized. Therefore, the adjustment angle of the “tibia” joint was set to its maximum opening degree, allowing us to further investigate the effective workspace range of both the “femur” joint and the “hip” joint. The geometric analysis of the “tibia” joint space activity is shown in **Fig. 7** (a). Due to the parallel structure, the spatial relationship between the plane containing *gh* and the plane containing ci is influenced solely by the opening angle of the PDCS. When the plane containing *gh* is parallel to the plane containing *ci*, $\angle gbc = 100^\circ$, $\angle gba = 30^\circ$, the angle γ is 73°, which can be obtained using Eq. 1:

$$\gamma = 360^\circ - 180^\circ - \angle edf - \angle fej - \angle fed = 110^\circ - \angle fej - \angle fed \quad (1)$$

where $\angle edf = \angle adc = \angle abc = 70^\circ$, $ef^2 = ed^2 + df^2 - 2ed \cdot df \cdot cos\angle edf$.

In the fabricated 3D-printed structure, the links ab and cd are designed with a finite width. When the PDCS moves to the position where the two links ab and cd come into contact, that is, when the height aa' of parallelogram $abcd$ with respect to base cd reaches 13mm, the PDCS attains its maximum opening angle. Substituting this value into Eq. 1 yields $\angle edf = 18^\circ$and $\gamma = 129^\circ$. Hence, the effective working angular range of the PDCS is determined to be from 73° to 129°.

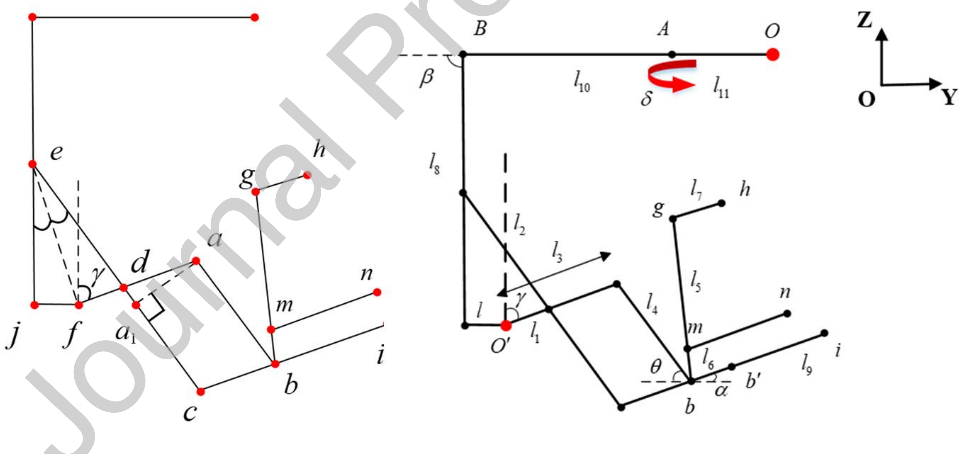

(a) Geometric analysis of the tibial joint; (b) Planar analysis of the grasping structure

Fig. 7. "Tibial joint" and grasping structure analysis diagrams.

Next, the activity angle of the "femur joint" during the formation of the grasping workspace is analyzed. As shown in **Fig. 7** (b), with the "hip joint" fixed at its initial position, the planar analysis diagram illustrates the projection of the grasping structure onto the YOZ plane. The arrow near point *A* and δ represent the counterclockwise rotation angle of the mechanical leg structure at point *A*. The projection function equation of the grasping structure on the YOZ plane is given as follows:

$$\begin{cases} l_{bg}: z_1 = -tan\left(\theta + \frac{\pi}{6}\right) \cdot (y_1 - y_b) + z_b\left(\theta + \frac{\pi}{3}\right) \\ y_1 = y_b\left(\theta + \frac{\pi}{3}\right) \\ l_{bi}: z_2 = tan(\alpha) \cdot (y_2 - y_b) + z_b \\ l_{mn}: z_3 = tan(\alpha) \cdot (y_3 - y_m) + z_m \\ l_{gh}: z_4 = tan\left(\frac{7\pi}{18} - \theta\right) \cdot (y_4 - y_g) + z_g \end{cases} \quad (2)$$

The relevant angle and coordinate expressions satisfy the following relationships:

$$\begin{cases} \gamma = \frac{2\pi}{3}, \alpha = \frac{\pi}{2} - \gamma, cos\theta = \frac{(l + l_1 \cdot cos\alpha)}{l_2} \\ y_b = l_3 \cdot cos\alpha + l_4 \cdot cos\theta, z_b = l_3 \cdot sin\alpha + l_4 \cdot sin\theta \\ y_g = y_b - l_5 \cdot cos\left(\theta + \frac{\pi}{6}\right), z_g = z_b + l_5 \cdot sin\left(\theta + \frac{\pi}{6}\right) \\ y_m = y_b - bm \cdot cos\left(\theta + \frac{\pi}{6}\right), z_m = z_b + bm \cdot sin\left(\theta + \frac{\pi}{6}\right) \end{cases} \quad (3)$$

Table I lists the constant segment lengths involved in the simulation. It is worth noting that when the angle of the "tibia joint" is determined, the transformation relationship between the $O' - xyz$ and $O - XYZ$ coordinate systems can be obtained using the following transformation matrix:

$$\begin{cases} R_{O'-B} = \begin{bmatrix} 1 & 0 & 0 \\ 0 & cos\left(\beta - \frac{\pi}{2}\right) & -sin\left(\beta - \frac{\pi}{2}\right) \\ 0 & sin\left(\beta - \frac{\pi}{2}\right) & cos\left(\beta - \frac{\pi}{2}\right) \end{bmatrix} \\ T_{O'-B} = [0 \quad -l_8 \cdot cos\beta + l \cdot sin\beta \quad -l_8 \cdot sin\beta - l \cdot cos\beta]^T \\ R_{B-O} = \begin{bmatrix} cos\delta & -sin\delta & 0 \\ sin\delta & cos\delta & 0 \\ 0 & 0 & 1 \end{bmatrix} \\ T_{B-O} = [0 \quad -l_{10} - l_{11} \quad 0]^T \end{cases} \quad (4)$$

TABLE I SIMULATION OF LINE SEGMENT CONSTANTS

Segment	Value/mm	Segment	Value/mm	Segment	Value/mm
l	20.3	l_4	53.6	l_8	121.5
l_1	20.0	l_5	72.3	l_9	52.0
l_2	65.8	l_6	11.4	l_{10}	98.1
l_3	53.7	l_7	25.0	l_{11}	39.0

In this paper, **Fig. 8** (a) illustrates the software simulation diagram, which depicts solely the effective portion of the grasping structure. The software simulation analysis revealed that the "three-finger" structure of the grasping mechanism started to intersect when the "femur" joint rotated, causing the "femur" link to swing from the horizontal position to approximately 86°. As the "three-finger" structure continued to rotate to about 95°, the degree of intersection reached its maximum, preventing further rotation. At this point, the dimensions of the effective grasping target were 74 mm*48 mm*21 mm.

In addition to the “femur” joint, the “hip” joint also contributes to the spatial flexibility of the grasping structure. When the “three-finger” structure intersects, the range of motion of the “hip” joint becomes constrained by this intersection. The simulation results revealed that the effective range of motion for the “hip” joint was -3° to 7°. **Fig. 8** (b)-(d) illustrate the left limit, right limit, and initial state of the workspace scope, respectively.

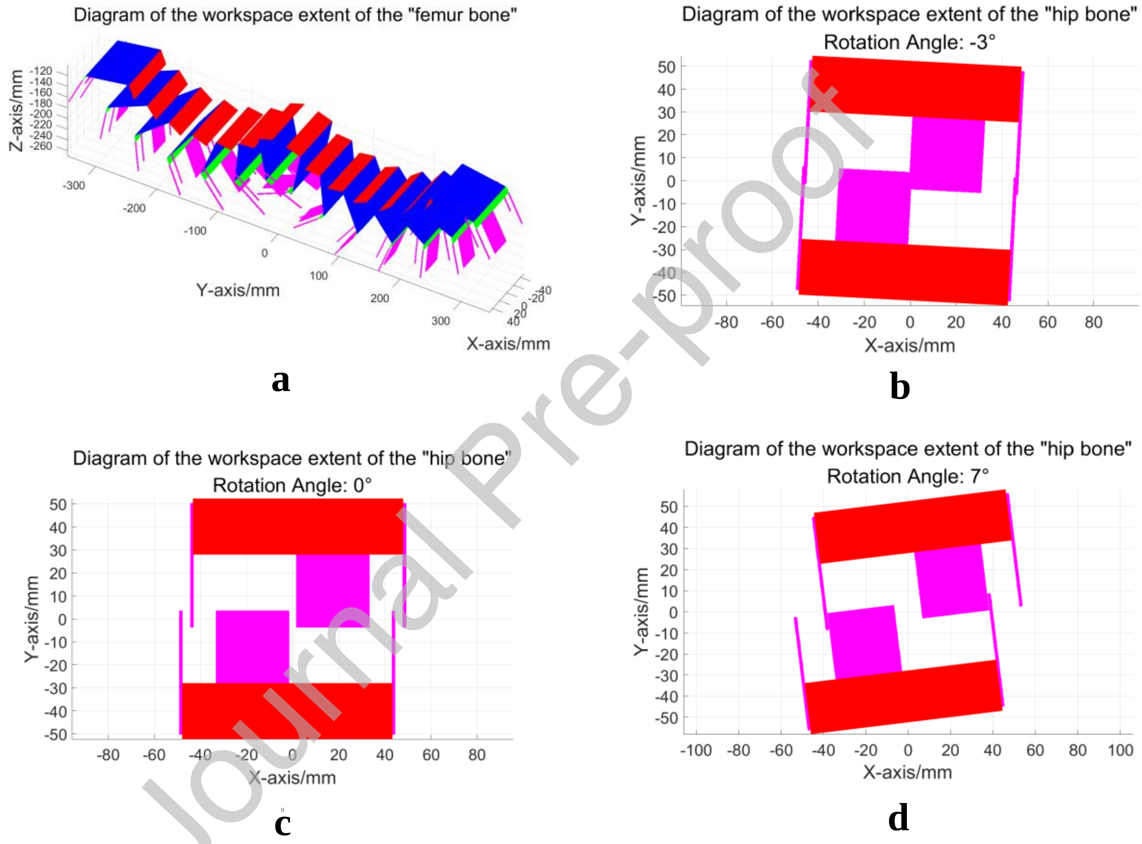

Fig. 8. The schematic diagram of the kinematic analysis: (a) The workspace simulation of the “femur joint”; (b) The workspace simulation of the “hip joint” (the left limit); (c) The workspace simulation of the “hip joint” (the right limit); (d) The workspace simulation of the “hip joint” (the initial state).

3.2. Static Stress Analysis

First and foremost, static stress analysis should focus on examining the primary contact surfaces and the key force-bearing components of the grasping structure during the grasping process. For the grasping structure, there are three distinct cases to consider. The schematic diagram of these three cases is presented in **Fig. 9**, where the lake blue object represents the object being grasped, and the red part highlights the primary contact area when grasping an object of that particular size. **Figs. 9** (a)-(c) correspond to the three cases of small, medium, and large object sizes, respectively. It is important to note that the blue cylinder depicted in the figure serves merely as an illustrative example of objects of varying volumes, used to determine the main force distribution areas within the grasping mechanism when handling objects of different sizes, rather than being limited to cylindrical objects alone.

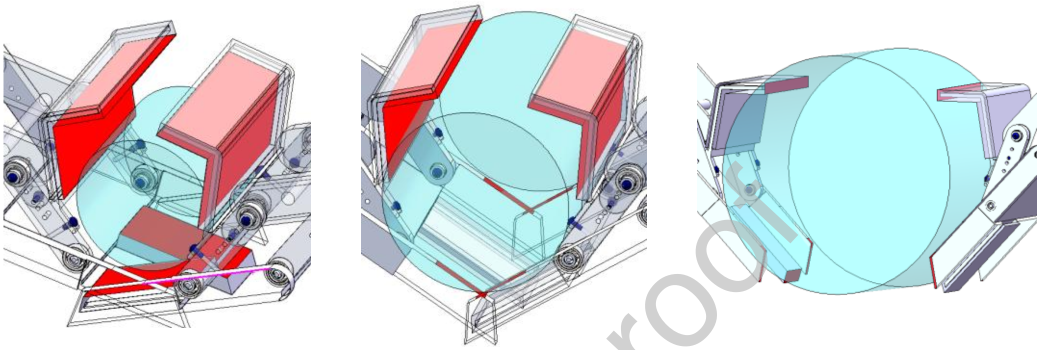

a b c

Fig. 9. The schematic of the grasping for the three cases: (a) Small size; (b)Middle size; (c) Large size.

In addition, when the grasping structure grasps the object, the slider will cause pressure on the rod. Therefore, it is also necessary to analyze the force of the rod. The following is the simulation analysis results of the two parts. Regarding the choice of material, the grasping structure, the slider accessories and rod connectors are made of ABS with a yield strength of 45 MPa. The slider rod is made of stainless steel with a yield strength of 137 MPa.

3.2.1. The static stress analysis of grasping structure

This simulation experiment mainly tested the load-bearing ability of a single grasping structure. A vertical force was applied to the middle "finger" region. The limiting case of applying force here could be obtained after several tests as shown in **Fig. 10**.

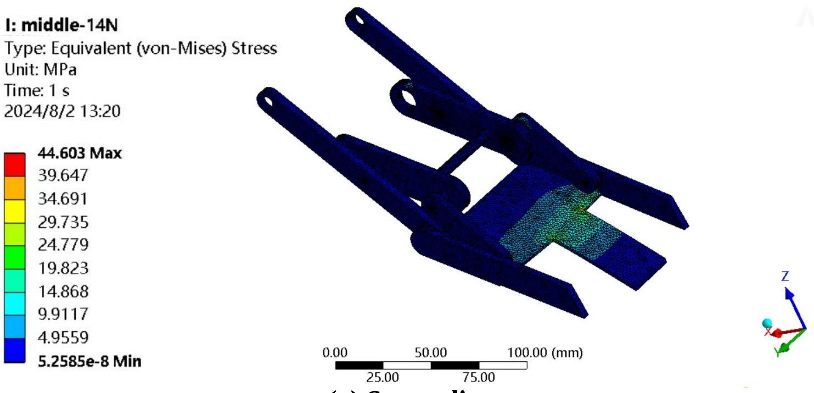

(a) Stress diagram

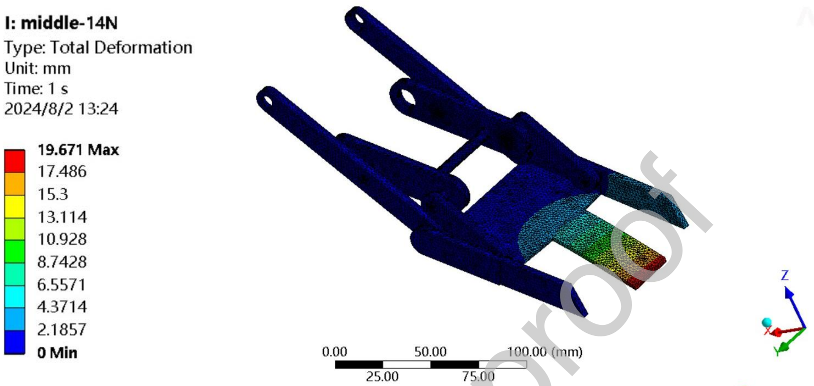

(b) Displacement diagram

Fig. 10. The simulation result diagram of static stress analysis I.

In this case, the magnitude of the applied force was 14 N, which was the maximum value. In **Fig. 10** (a), the place where the maximum stress was indicated was the junction of the middle “finger” and “palm”. The maximum stress was 44.6 MPa. In **Fig. 10** (b), the maximum deformation was 19.7 mm at the fingertip of the middle “finger”. However, there were no nonzero values in the equivalent plastic strain map.

Then, considering the grasping situation of an object of medium size, forces in the vertical direction of the two contact surfaces were given to the middle areas of the outer “two-finger”. The limiting case of applying force here could be obtained after several tests as shown in **Fig. 11**.

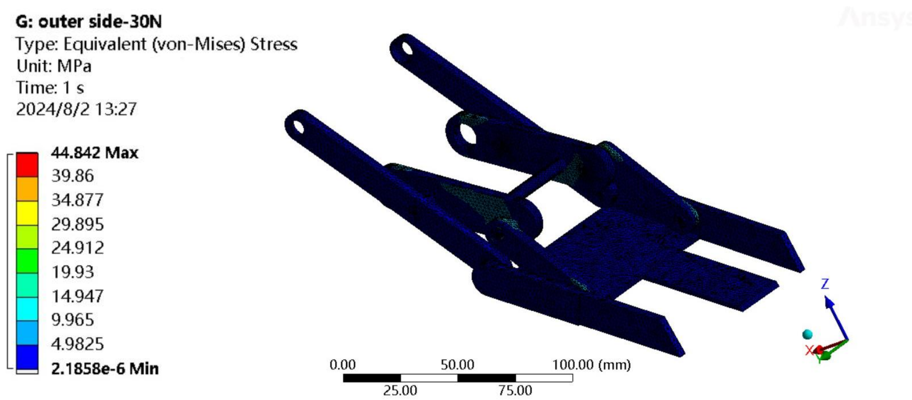

(a) Stress diagram

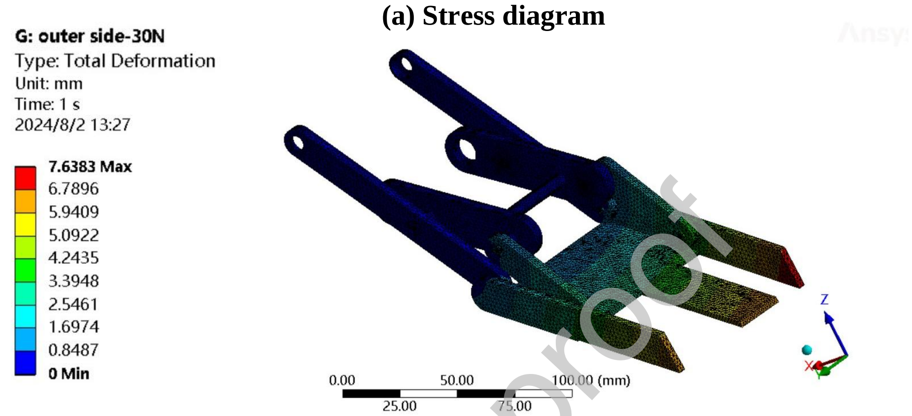

(b) Displacement diagram

Fig. 11. The simulation result diagram of static stress analysis II.

In this case, a total of 30N forces were applied. The place with the maximum stress in **Fig. 11** (a) was the place where L_1 and L_2 were connected. The maximum stress value of the stress diagram was 44.8 MPa. In **Fig. 11** (b), the maximum deformation was 7.6 mm at the end of the grasp. There were no nonzero values in the equivalent plastic strain map.

Finally, considering the case of grasping a large size object, a force in the vertical direction was applied to the two terminal contact surfaces of the “two fingers” on the outer side of the “three-finger” structure. The limiting case of applying force here could be obtained after several tests as shown in **Fig. 12**.

In this case, the total force applied was 25 N. The place with the maximum stress in **Fig. 12** (a) was the place where L_1 and L_2 were connected as well. The maximum stress value of the stress diagram was 44.1 MPa. In **Fig. 12** (b), the maximum deformation was 7.5 mm at the end of the grasp. There were no nonzero values in the equivalent plastic strain map.

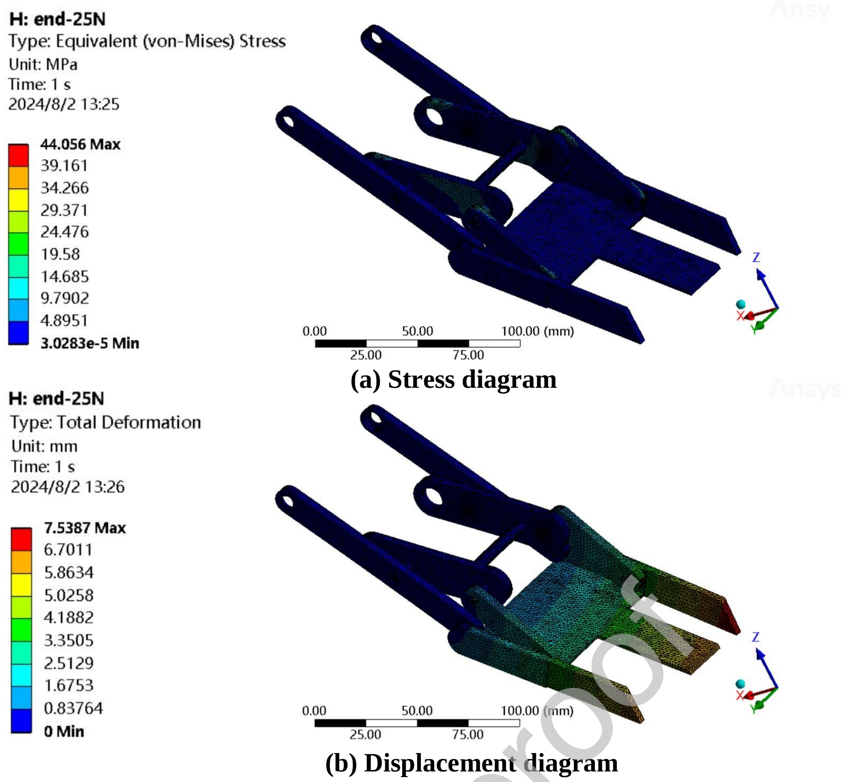

Fig. 12. The simulation result diagram of static stress analysis III.

3.2.2. The static stress analysis of slider

After giving a vertical sliding rod direction force at the connection between the slider and the connecting rod, the limiting case of applying force here could be obtained after several tests as shown in **Fig. 13**.

In this case, the total force applied was 16 N. The **Fig. 13** (a) indicated that the maximum stress was at the chute where the slider contacted the slider rod. The maximum value was 69.8 MPa. There was also no red area (greater than 45 MPa) in the ABS material section. In **Fig. 13** (b), the maximum displacement was 2.9 mm. Although the load-bearing limit of the slider part is not high, the driving servo provides the main force and torque to offset the impact of the target object during grasping. Therefore, the pressure on the slider part is not significant, and the load-bearing does not affect the actual grasping.

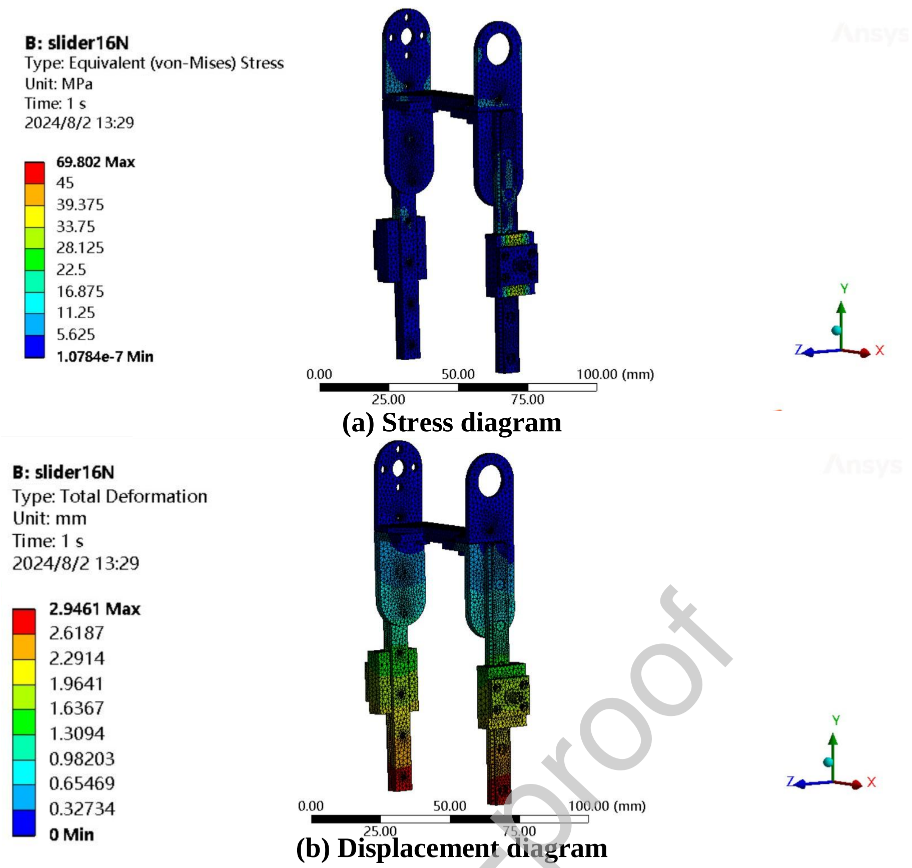

Fig. 13. The simulation result diagram of static stress analysis IV.

4. Experimental Results

Our team used 3D printing technology to complete the manufacturing of mechanical legs. Below is a detailed overview of the specific experimental procedure.

4.1. Experiments on Grasping Ability and Load Capacity

After installing the mechanical leg onto the robot, a small metal box was used in this study to evaluate the maximum capacity of the grasping structure, fabricated using 3D materials, for objects of specific weights. The upper limit of the grasping structure's ability to hold the target was determined by continuously adding counterweight iron pieces, each weighing 50 g. **Fig. 14** illustrates the diagram depicting the iron sheet reaching the maximum counterweight and the schematic representation of the robot's grasping situation during the experiment. The experimental results indicate that the grasping structure exhibited a maximum grasp capacity of approximately 22.5 N when using 3D printing materials.

During actual robot movement, the acceleration exerts a greater force on the paw than the weight of the object to be grasped. Consequently, the upper limit of the grasping structure's ability to hold the target object will be less than 22.5 N in such cases. However, due to constraints related to the experimental site and available laboratory equipment, we only tested the maximum grasping capacity of the structure in the robot's static state. Additionally, considering the robot's weight of 9.5 kg, the acceleration provided by the thrusters for continuous upward movement over a period of time will not exceed 1 m/s². Even in the extreme case of 1 m/s², the influence of motion on the grasping capacity is minimal.

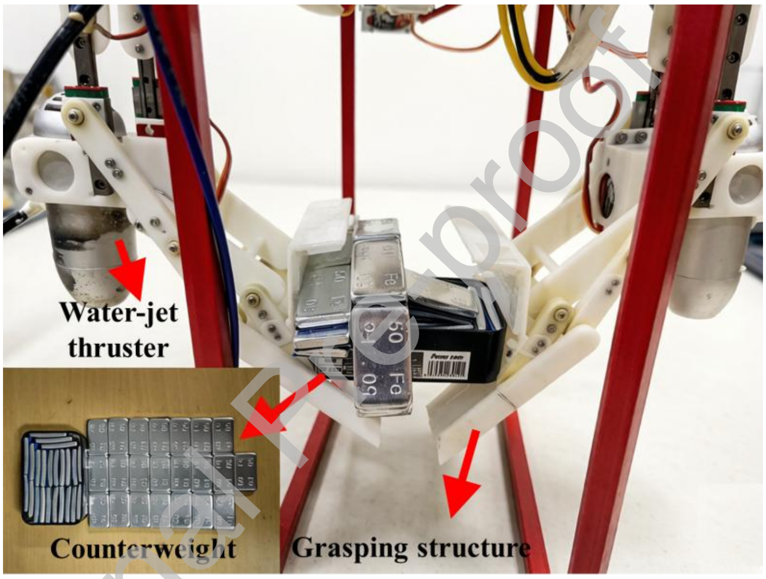

Fig. 14. The experimental graph of the upper limit of grasping ability.

The following is an assessment of the robot's loading capacity in water. Considering the movement task after grasping, two of the robot's mechanical legs are required to control its motion, while the other two mechanical legs are responsible for the grasping task. For efficient and convenient testing, the robot's grasping structure was rotated to 90°. The thruster speed was adjusted to a high value capable of sustaining the robot's operation for a specific duration. In this experiment, underwater movement is achieved by changing the thrust of the water-jet thrusters. The load was incrementally increased by continuously adding counterweight iron pieces above the robot, each weighing 50 g. The maximum load capacity of the robot was determined based on its ability to remain suspended after the addition of the iron pieces. **Fig. 15** illustrates the diagram of the robot's load reaching the upper limit of the counterweight. According to the experimental results, the robot's upper load limit in water is 6 N, at which point the robot was in a state of equilibrium, neither sinking nor rising.

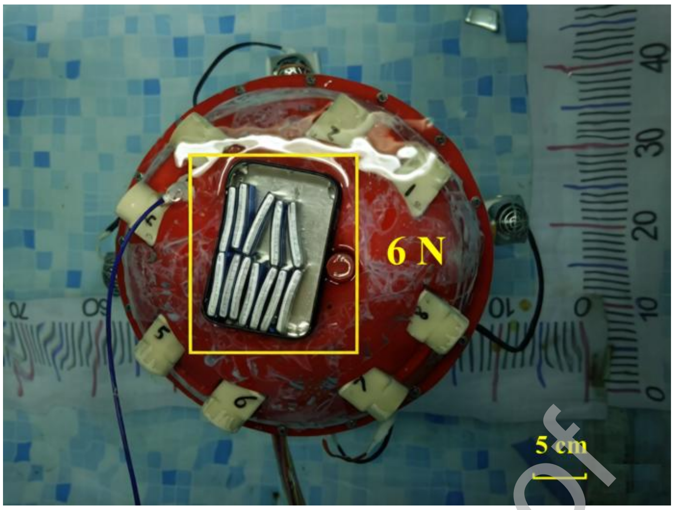

Fig. 15. The experimental diagram of the upper limit of load capacity.

4.2. Grasping Adaptability Experiments

The next step involves testing the grasping adaptability of the grasp structure to various types of target objects. Our team selected a diverse range of objects for underwater grasping experiments. The schematic diagram illustrating the various types of objects is presented in **Fig. 16**.

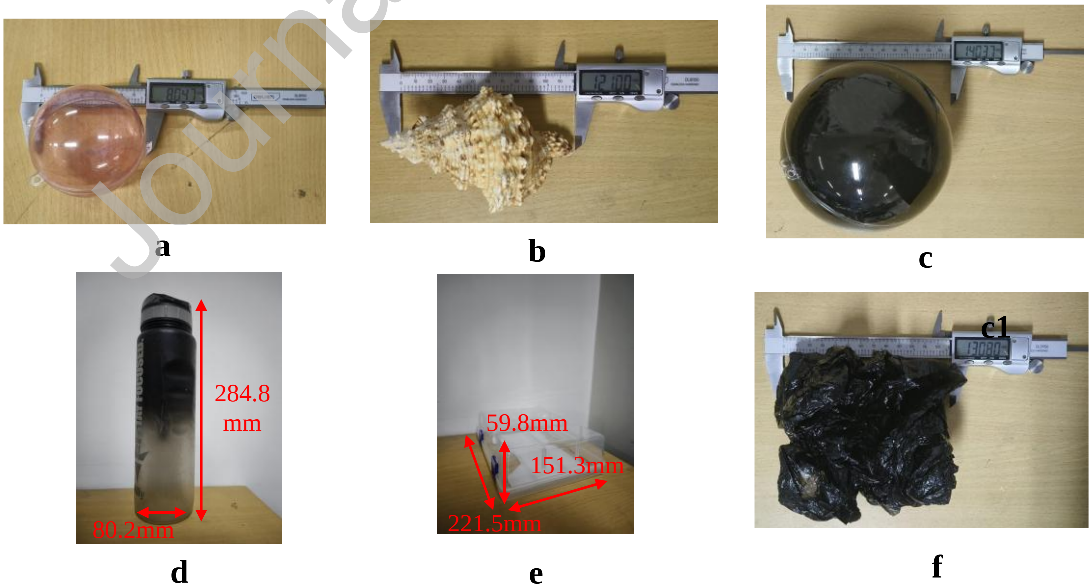

Fig. 16. The diagram of grabbing the object: (a) A small smooth acrylic ball; (b) A conch; (c) A large smooth acrylic ball; (d) A vertical cylinder; (e) A rectangular box; (f) A plastic bag.

Among these, object a represents a small-sized and smoothly regular object, while object b represents a medium-sized and roughly irregular object. Objects c, d, and e represent large-sized and smoothly regular objects, whereas object f represents a flexible and deformable irregular item. Given the scenario where the robot system replaces divers for collecting marine creatures and cleaning up marine debris, we have chosen a conch as item b and a plastic bag as item f. To assess the grasping effect of friction when handling large-volume items, we selected a vertical cylinder as item d and a rectangular box as item e.

Since the primary objective of this underwater grasping experiment was to validate the grasping characteristics of the newly designed mechanical leg, its performance was evaluated based on its ability to successfully grasp various types of objects. Consequently, manual intervention was employed for motion control during the grasping process, rather than automatic control. **Fig. 17** provides a top view of the grasping experiment area, clearly marking the placement of the underwater camera, the position of the objects to be grasped, and the target area where the robot intends to move after grasping the object. Besides, Figure 16 also presents a schematic diagram illustrating the dimensions of the target area, which measures approximately 500.0 mm by 500.0 mm.

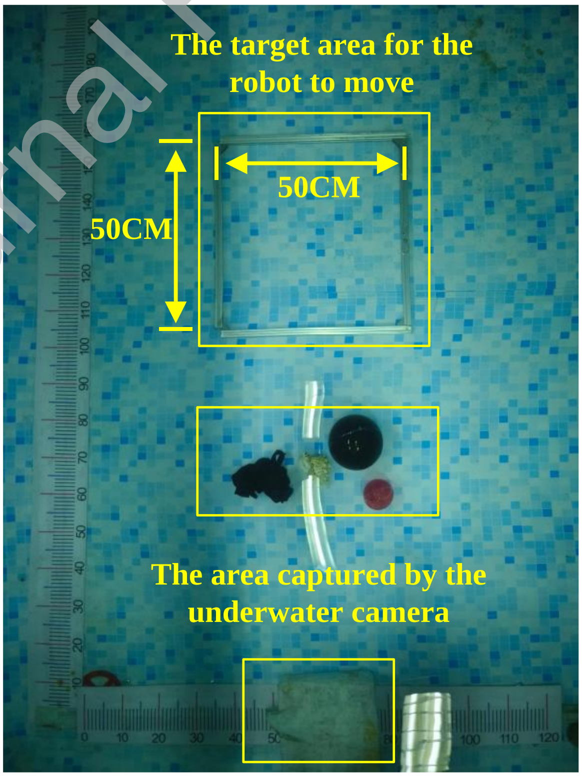

Fig. 17. The top view of the grasping experiment area.

In the grasping experiments, a total of seven sets of 20 trials each were conducted on six different types of objects. During these experiments, the target objects were submerged to the bottom and maintained in a stationary position. A grasp was considered successful if the robot was able to pick up the object and move it to the target area. Conversely, if the robot failed to grasp the target object or if the object dislodged from the mechanical claw during transport, the grasping action was deemed unsuccessful. The statistical plot depicting the number of successful grasps in the experiment is shown in **Fig. 18**. According to the statistical graph, the overall success rate of the grasping experiments was high.

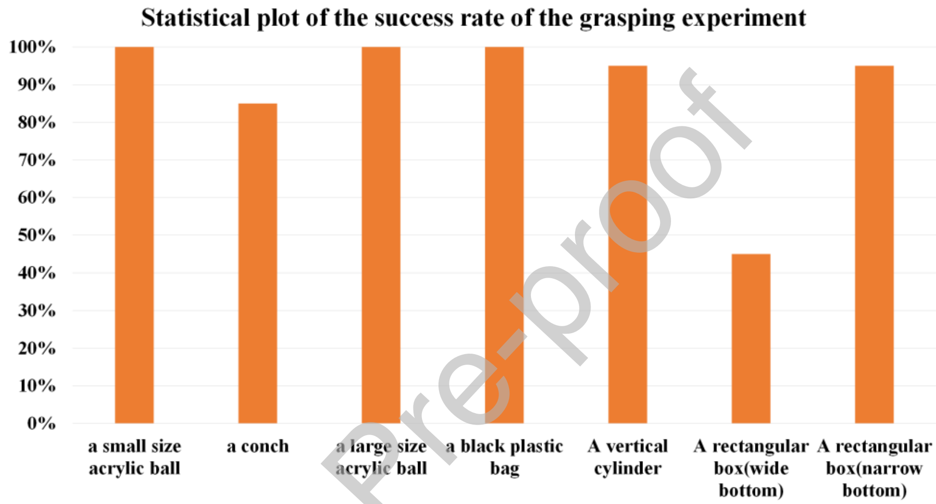

Fig. 18. Statistical plot of the grasping experiment.

The mechanical claw easily grasped the center of gravity of the target due to the regular shape of the acrylic ball, the ease of deformation, and the large surface area of the plastic bag, making a 100% success rate credible. However, the irregular shape of the conch made it difficult to locate the center of gravity during manual positioning, leading to grasping failures, and thus, an 85% success rate is also considered credible. Although the vertical cylindrical water bottle primarily relies on a minimal contact surface for friction, the grasping structure provided a superior clamping effect, resulting in a trustworthy 95% success rate for lightweight water bottles.

The experiment involved gripping a rectangular box in two different orientations: one with the narrow face submerged in water as the bottom, and the other with the wide face submerged. In the first scenario, the grasping end had a larger contact area to generate friction, resulting in an effective double-clamping effect and supporting a 95% success rate. However, in the second scenario, the grasping end faced challenges in lifting or gripping the box due to the limited contact area providing friction, leading to a success rate of less than 60%. It is also worth noting that the influence of object weight on the mechanical leg was mainly reflected in the uniformity of weight distribution. When the weight was unevenly distributed, the grasping success rate fell below 75%. In contrast, for objects with a regular shape and a weight within the load-bearing capacity of the mechanical leg, the success rate exceeded 90%.

During the process of grasping the target object, we identified five factors that may contribute to unsuccessful grasping. Firstly, the position of the object can be altered by changes in water flow around it when the mechanical leg opens to grasp. Secondly, the water jet from the thruster can also induce changes in water flow, subsequently affecting the object's position. Thirdly, manual errors may arise when aligning the robot with the target object, leading to misalignment. Fourthly, significant weight distribution imbalances in the grasped object can impede the mechanical leg's ability to accurately grasp key areas. Lastly, relying solely on friction from a single end may be inadequate for gripping large objects.

The first factor has minimal impact due to the slow opening of the mechanical leg. Similarly, the second factor has negligible influence as the water jet direction of the thruster does not align with the direction of the grasped object. Both the third and fourth factors are primarily attributed to misalignment between the mechanical leg and the center of gravity of the target object, serving as the main causes of failure. The fifth factor primarily applies to bulky and heavy objects.

The detailed experimental procedure can be found in the supplementary materials. In the underwater experiment, the robot initially grasps the target object and then navigates to the designated area while maintaining its grip. To illustrate each stage of the grasping experiment, we take the example of grasping a small red ball.

In **Fig. 19**, Group A graphs depict the grasping process of each object as recorded by the underwater camera during the experiment. Group B graphs, on the other hand, illustrate the robot's process of transporting the grasped objects to the target area behind it and subsequently releasing them. The five images in Group A represent the five stages of preparation, opening of the grasping structure, approaching the target, initial grasping of the target, and complete grasping of the target. Similarly, the five images in Group B represent the five stages of the initial state, continuous approach to the target area, arrival above the target area, release of the target object, and completion of the grasping structure's contraction.

A

B

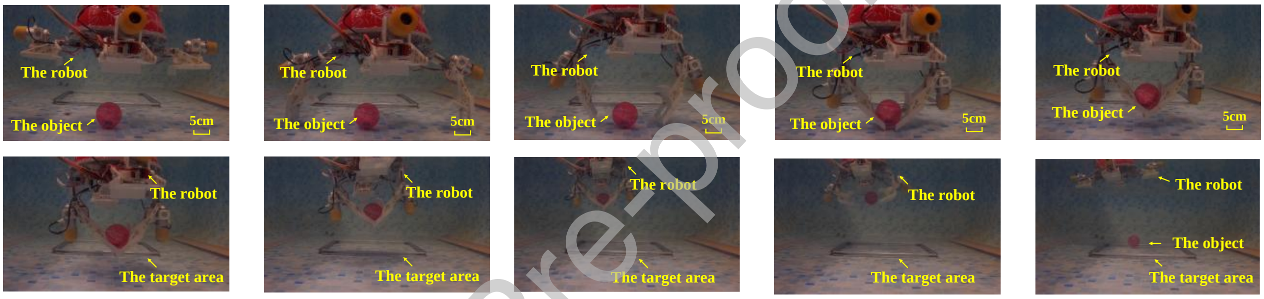

Fig. 19. The diagrams of grasping experiment (the smooth red small size acrylic ball)

The experimental results of the grasping tasks demonstrate that the grasping structure has successfully completed the task for each target object in the experimental scheme. These results indicate that the new mechanical leg proposed in this paper has successfully integrated the grasping function to a certain extent.

4.3. Land Crawling Experiments

After the installation of the new mechanical leg, the robot's swimming experiment in water exhibited a similar movement pattern to its predecessor, as evidenced by the aforementioned grasping experiment. Achieving precise control over the robot's motion solely requires refining the control algorithm, which is beyond the scope of this paper. However, on land, the crawling experiment was influenced by both a reduction in movable joints and an increase in single leg volume due to the mechanical leg modifications. This subsection empirically evaluates the robot's crawling function using three different gait cycles. The experimental setup is illustrated in **Fig. 20** (a), while **Fig. 20** (b) presents the velocity statistics for the different gait cycles. These results indicate that the robot still possesses some crawling ability.

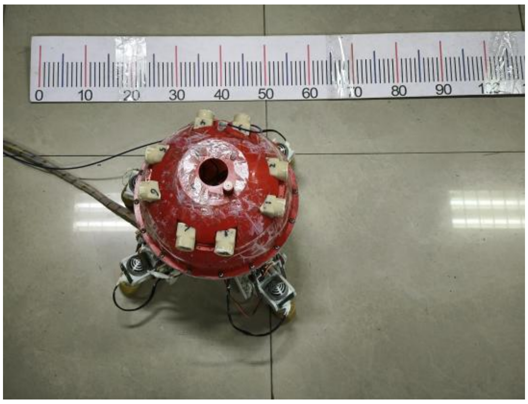

a

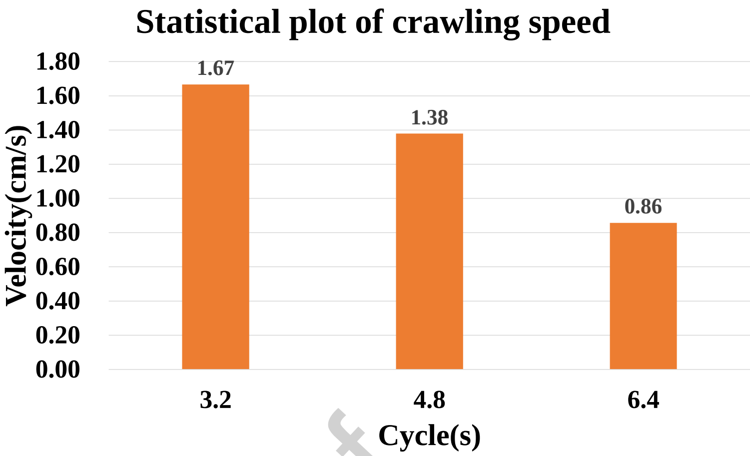

b

Fig. 20. The diagrams of clamping experiment: (a) The experimental scene; (b) The statistical plot of crawling speed.

The crawling experiment of the robot can be seen in the supplementary video. Based on the outcomes of the crawling experiment, it is evident that the robot's crawling speed has decreased. This reduction can be primarily attributed to the modifications in the leg structure, which have affected the step length settings during the robot's gait design. Specifically, within the same gait cycle, a decrease in step length has resulted in a corresponding decrease in speed. Notwithstanding, as observed in the experimental video, the robot retains its crawling capability, thereby adequately demonstrating its crawling proficiency.

5. Discussion

Based on the analysis of the simulation and grasping experiments conducted on the new mechanical leg mentioned above, the following points merit attention and discussion:

(1)Material selection for the new mechanical leg. In consideration of production convenience and cost-effectiveness, our team temporarily selected a type of resin (ABS-like material) for the manufacturing of the grasping structure. This material allows a single grasping structure to withstand a vertical downward force of up to 30 N. However, the actual load-bearing capacity is influenced by the specifications of the servo and power consumption. Meanwhile, some high-strength, lightweight aluminum alloys could potentially yield better experimental performance.

(2) Load capacity of the robot. The robot's load capacity is primarily supported by the thruster. In this study, the maximum load capacity of the robot in water is 6 N. In the future, the load capacity can be increased by adjusting the thrust of the water-jet thruster according to actual operational requirements.

(3) Robot grasping experiment design. The experiment primarily focused on evaluating the structure's grasping capability across various types of objects. The experimental process of the robot grasping the target object is shown in **Fig. 21**. Therefore, the high experimental success rate observed in this context is both credible and effective. However, the implementation of the robot's grasping function still necessitates autonomous target localization, which will be addressed in our subsequent experimental research. The achievement of a high grasping success rate in this context will be a crucial indicator. The grasping adaptability of the robot is analyzed in **Fig. 22**, and the volume constraints for objects of varying shapes is discussed. Based on the grasping characteristics of the structure, the primary consideration was to derive cube models that are tangent to the main section of the target object from different shapes. Subsequently, different volume limits were determined based on the varying contact surfaces between the cube and the grasping structure. In conjunction with the analysis of the three contact conditions presented in *Section III*, the upper limit for the first case is 85 mm*85 mm*85 mm. When any dimension along the XYZ axis exceeds 85 mm, the second case must be considered for application. In the second case, we set the upper bound of the X-axis to be no larger than the robot's size. When the XYZ dimensions of the target object surpass the corresponding upper bound size of the second case, the third case is considered. In the third case, due to the minimal contact area between the grasping structure and the target, the focus is primarily

on targets with large volumes but relatively light weights. For such objects, weight becomes the key consideration. Therefore, the target volume limit in this case is not discussed. The discussion regarding the upper limit of the target grasping weight is elaborated upon in the static stress analysis in *Section III* and the experiments in *Section IV*.

Fig. 21. The experimental process of the robot grasping the target object.

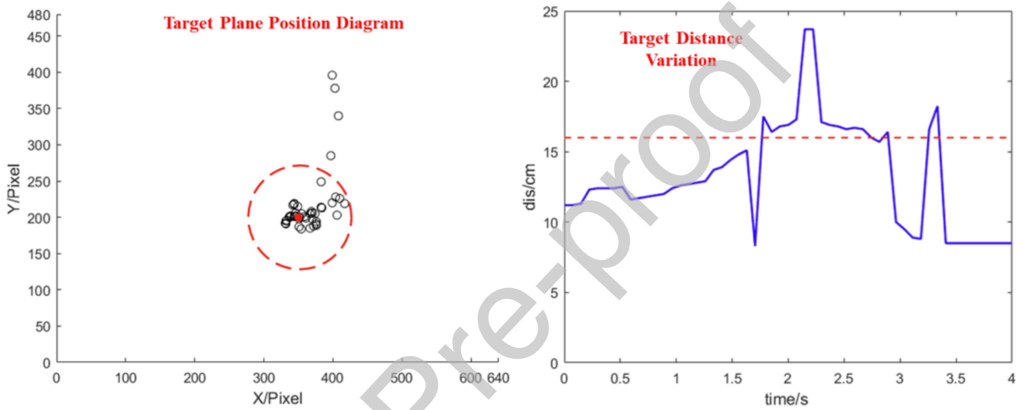

Fig. 22. The grasping adaptability of the robot.

(4)The movement mode of the robot. This study represents a comprehensive exploration centered around the amphibious robot platform. Building upon the previous generation of robots, which successfully demonstrated underwater parading and land crawling capabilities, this paper introduces the grasping function of the newly designed mechanical leg. The structural modifications of this new mechanical leg are primarily discussed in the context of underwater swimming and land crawling, without delving into intricate theoretical analyses or control methodologies. The new legs are designed to preserve as much as possible the water swimming and land crawling capabilities of their predecessors, thereby showcasing the effective integration of three key functions: underwater grasping, underwater swimming, and land crawling.

(5)The versatility of robots. In contrast to other robotic platforms that often incorporate separate robotic arms for grasping, leading to increased overall volume. To address this limitation and enhance versatility, we have focused on developing a unified structural unit that integrates grasping functionality directly into the robot's motion module. By leveraging the existing structure of the motion module and extending it to incorporate a contraction mechanism that also serves as a grasping device, we have successfully multi-functionalized a single component. Our experimental results demonstrate the robot's ability to perform a range of tasks, including crawling on the ground, swimming in water, and grasping objects within aquatic environments, all while maintaining a compact design. This integrated approach represents a significant advancement in robotic versatility and functionality.

6. Conclusions and Future Work

Based on a bionic amphibious robot platform, this paper presents an innovative modification of the leg mechanism that integrates a grasping function while preserving the robot's original capabilities for terrestrial crawling and underwater locomotion. This design achieves multifunctional reuse of a single mechanical structure, significantly enhancing the robot's operational flexibility and concealment. By exploiting the deformation characteristics of a PDCS and incorporating a sliding pair structure, the grasping mechanism is effectively combined with the joint of the mechanical leg. A series of simulations and grasping experiments demonstrate that the proposed structure successfully integrates the grasping function and exhibits good adaptive grasping performance underwater. Future work will further optimize the sensing capabilities and grasping control of this structure to achieve autonomous and precise underwater grasping.

Acknowledgment

This work was supported in part by the GuangDong Basic and Applied Basic Research Foundation General Program under Grant 2025A1515011007, in part by Shenzhen Science and Technology Program under Grant RCBS20231211090725048, and in part by the High level of special funds from Southern University of Science and Technology under Grant G03034K003.

References

[1] C. Jiang, X. Xiong, X. Xiang, Z. Zeng and F. Zhang, "Underwater Perception and Autonomous Operation for Underwater Vehicle-Manipulator Systems: Methodology and Experiment," *IEEE/ASME Transactions on Mechatronics*, vol. 30, no. 6, pp. 5029-5040, 2025.

[2] A. Li, S. Guo, C. Li, H. Yin; M. Liu; L. Shi, "A Moving Obstacle Avoidance Strategy-Based Collaborative Formation for the Bionic Multi-Underwater Spherical Robot Control System," *Ocean Engineering*, vol. 329, p. 121120, 2025.

[3] Z. Tu, Y. Zhu, X. Wu and C. Yang, "A Unified Shared Control Architecture for Underwater Vehicle-Manipulator Systems Using Task Priority," *Frontiers of Information Technology & Electronic Engineering*, vol. 26, no. 8, pp. 1411-1427, 2025.

[4] C. Li, and S. Guo, "Characteristic evaluation via multi-sensor information fusion strategy for spherical underwater robots," *Information Fusion*, vol. 95, pp. 199-214, Jul. 2023.

[5] M. Cai, Y. Wang, S. Wang, R. Wang and M. Tan, "Autonomous Manipulation of an Underwater Vehicle-Manipulator System by a Composite Control Scheme With Disturbance Estimation," *IEEE Transactions on Automation Science and Engineering*, vol. 21, no. 1, pp. 1012-1022, 2024.

[6] X. Bai, Y. Wang, R. Wang, S. Wang and M. Tan, "Hydrodynamics of a Flexible Flipper for an Underwater Vehicle-Manipulator System," *IEEE/ASME Transactions on Mechatronics*, vol. 27, no. 2, pp. 868-879, 2022.

[7] Y. Wang, M. Cai, S. Wang, X. Bai, R. Wang and M. Tan, "Development and control of an underwater vehicle-2manipulator system propelled by flexible flippers for grasping marine organisms," *IEEE Transactions on Industrial Electronics*, vol. 69, no. 4, pp. 3898-3908, 2020.

[8] Y. Maezawa, Y. Ambe, Y. Yamauchi, M. Konyo, K. Tadakuma and S. Tadokoro, "Translational Disturbance Rejection for Jet-Actuated Flying Continuum Robots on Mobile Bases," *IEEE Robotics and Automation Letters*, vol. 8, no. 11, pp. 7456-7463, 2023.

[9] G. Brantner, and Khatib O, "Controlling Ocean One: Human-robot collaboration for deep‐sea manipulation", *Journal of Field Robotics*, vol. 38, no. 1, pp. 28-51, 2021.

[10] C. Li, J. Long and S. Guo, "Modeling and Performance Evaluation of a Novel Bioinspired Ellipsoidal Underwater Robot," *IEEE Journal of Oceanic Engineering*, vol. 50, no. 4, pp. 2720-2731, 2025.

[11] A. Li, S. Guo and C. Li, "An Improved Motion Strategy With Uncertainty Perception for the Underwater Robot Based on Thrust Allocation Model," *IEEE Robotics and Automation Letters*, vol. 10, no. 1, pp. 64-71, 2025.

[12] R. Baines, S. Patiballa, J. Booth, L. Ramirez, T. Sipple, A. Garcia, F. Fish, R. Kramer-Bottiglio, "Multi-environment robotic transitions through adaptive morphogenesis," *Nature*, vol. 610, no. 7931, pp. 283-289, 2022.

[13] A. Liu, X. Zhang, H. Huang, F. Xiao, Z. Zhang, G. Cui, "An Intelligent Bionic Amphibious Turtle Robot With Visual-Tactile Fusion for Dynamic Terrain Adaptation," *IEEE Transactions on Robotics*, vol. 41, pp. 6345-6363, 2025.

[14] S. Gu, L. Zhang, S. Guo, L. Zheng, R. An, T. Jiang, "Communication and Cooperation for Spherical Underwater Robots by Using Acoustic Transmission," *IEEE/ASME Transactions on Mechatronics*, vol. 28, no. 1, pp. 292-301, 2023.

[15] R. An, S. Guo, L. Zheng, H. Hirata, S. Gu, "Uncertain moving obstacles avoiding method in 3D arbitrary path planning for a spherical underwater robot," *Robotics and Autonomous Systems*, vol. 151, p. 104011, 2022.

[16] R. An, S. Guo, Y. Yu, C. Li, and T. Awa, "Task planning and collaboration of jellyfish-inspired multiple spherical underwater robots," *Journal of Bionic Engineering*, vol. 19, no. 3, pp. 643-656, May. 2022.

[17] H. Yin, S. Guo, A. Li, L. Shi, and M. Liu, "A Deep Reinforcement Learning-based Decentralized Hierarchical Motion Control Strategy for Multiple Amphibious Spherical Robot Systems with Tilting Thrusters", *IEEE Sensors Journal*, vol. 24, no. 1, pp. 769-779, 2023.

[18] H. Yin, S. Guo, and M. Liu, "A virtual linkage-based dual event-triggered formation control strategy for multiple amphibious spherical robots in constrained space with limited communication," *IEEE Sensors Journal*, vol. 22, no. 13, pp. 13395-13406, 2022.

[19] S. Guo, S. Cao, and J. Guo, "Study on decentralization of spherical amphibious multi-robot control system based on smart contract and blockchain," *Journal of Bionic Engineering*, vol. 18, no. 6, pp. 1317-1330, 2021.

[20] R. Wang, J. Wang, Z. Zhu and D. Wang, "Multimodal Magnetic Soft Robots Enabled by Bistable Kirigami Patterns," *IEEE/ASME Transactions on Mechatronics*, vol. 29, no. 6, pp. 4526-4537, 2024.

[21] J. Wan, L. Sun and T. Du, "Design and Applications of Soft Actuators Based on Digital Light Processing (DLP) 3D Printing," *IEEE Access*, vol. 11, pp. 86227-86242, 2023.

[22] Y. Fei, J. Wang, and W. Pang, "A novel fabric-based versatile and stiffness-tunable soft gripper integrating soft pneumatic fingers and wrist," *Soft robotics*, vol. 6, no. 1, pp. 1-20, Feb. 2019.

[23] M. Wu, X. Zheng, R. Liu, N. Hou, W. Afridi, R. Afridi, X. Guo, J. Wu, C. Wang, G. Xie, "Glowing Sucker Octopus (Stauroteuthis syrtensis)-Inspired Soft Robotic Gripper for Underwater Self-Adaptive Grasping and Sensing," *Advanced Science*, vol. 9, no. 17, 2022.

[24] J. Liu, Z. Song, Y. Lu, H. Yang, X. Chen, Y. Duo, B. Chen, S. Kong, Z. Shao, Z. Gong, S. Wang, X. Ding, J. Yu, L. Wen, "An Underwater Robotic System With a Soft Continuum Manipulator for Autonomous Aquatic Grasping," *IEEE/ASME Transactions on Mechatronics*, vol. 29, no. 2, pp. 1007-1018, 2024.

[25] K. Nishi, M. Kobayashi and Y. Uranishi, "MR-UBi: Mixed Reality-Based Underwater Robot Arm Teleoperation System With Reaction Torque Indicator via Bilateral Control," *IEEE Access*, vol. 14, pp. 40137-40146, 2026.

[26] J. Liu, S. Iacoponi, C. Laschi, L. Wen and M. Calisti, "Underwater Mobile Manipulation: A Soft Arm on a Benthic Legged Robot", *IEEE Robotics & Automation Magazine*, vol. 27, no. 4, pp. 12-26, 2020.

[27] A. Li, S. Guo and C. Li, "An Artificial Lateral Lines-based an Active Obstacle Recognition Strategy and Performance Evaluation for Bionic Underwater Robots," *IEEE Sensors Journal*, vol. 24, no. 16, pp. 26266-26277, 2024.

[28] H. Xing, C. Liu, S. Guo, L. Shi, W. Liu, H. Li, Y. Zhao, "Research on Multi-mode Motion of the Miniature Amphibious Turtle-inspired Robot", *Robot*, vol. 44, no. 2, pp. 212-223, 2022.

[29] C. Gu, S. Guo, M. Liu, H. Yin, A. Li, "Design and Characteristic Evaluation of a Novel Clamping Mechanism for Amphibious Spherical Bionic Robots," *in proceedings of 2023 IEEE International Conference on Mechatronics and Automation (ICMA)*, Harbin, China, 2023, pp. 1935-1940.

[30] H. Xing, L. Shi, X. Hou, Y. Liu, Y. Hu, D. Xia, Z. Li, S. Guo, "Design, Modeling and Control of a Miniature Bio-inspired Amphibious Spherical Robot", *Mechatronics*, vol. 77, p. 102574, 2021.

Declaration of interests

☒ The authors declare that they have no known competing financial interests or personal relationships that could have appeared to influence the work reported in this paper.